Noninvasive imaging of human skin hemodynamics using a digital red-green-blue camera

Izumi Nishidate
Noriyuki Tanaka
Tatsuya Kawase
Takaaki Maeda
Tomonori Yuasa
Yoshihisa Aizu
Tetsuya Yuasa
Kyuichi Niizeki

Noninvasive imaging of human skin hemodynamics using a digital red-green-blue camera

Izumi Nishidate,[a] **Noriyuki Tanaka,**[a] **Tatsuya Kawase,**[a] **Takaaki Maeda,**[b] **Tomonori Yuasa,**[c] **Yoshihisa Aizu,**[c] **Tetsuya Yuasa,**[d] **and Kyuichi Niizeki**[d]

[a]Tokyo University of Agriculture & Technology, Graduate School of Bioapplications and Science Engineering, Koganei, Tokyo 184-8588, Japan
[b]Kushiro National College of Technology, Department of Mechanical Engineering, Kushiro, Hokkaido 084-0916, Japan
[c]Muroran Institute of Technology, College of Design and Manufacturing Technology, Muroran, Hokkaido 050-8588, Japan
[d]Yamagata University, Graduate School of Biosystem Engineering, Yonezawa, Yamagata 992-8510, Japan

Abstract. In order to visualize human skin hemodynamics, we investigated a method that is specifically developed for the visualization of concentrations of oxygenated blood, deoxygenated blood, and melanin in skin tissue from digital RGB color images. Images of total blood concentration and oxygen saturation can also be reconstructed from the results of oxygenated and deoxygenated blood. Experiments using tissue-like agar gel phantoms demonstrated the ability of the developed method to quantitatively visualize the transition from an oxygenated blood to a deoxygenated blood in dermis. *In vivo* imaging of the chromophore concentrations and tissue oxygen saturation in the skin of the human hand are performed for 14 subjects during upper limb occlusion at 50 and 250 mm Hg. The response of the total blood concentration in the skin acquired by this method and forearm volume changes obtained from the conventional strain-gauge plethysmograph were comparable during the upper arm occlusion at pressures of both 50 and 250 mm Hg. The results presented in the present paper indicate the possibility of visualizing the hemodynamics of subsurface skin tissue. © *2011 Society of Photo-Optical Instrumentation Engineers (SPIE)*. [DOI: 10.1117/1.3613929]

Keywords: skin tissue; blood; hemoglobin; oxygen saturation; RGB image; Monte Carlo simulation; strain-gauge plethysmograph; upper arm occlusion.

Paper 11113R received Mar. 9, 2011; revised manuscript received Jun. 5, 2011; accepted for publication Jun. 27, 2011; published online Aug. 5, 2011.

1 Introduction

Quantitative assessment of human skin hemodynamics, such as blood perfusion and its oxygenation state, is important for monitoring tissue metabolism and health status, diagnosis of allergic dermatitis, and evaluating tissue viability in surgery and convalescence. The diffuse reflectance spectrum of human skin reflects the optical absorption spectra of chromophores (i.e., oxygenated hemoglobin, deoxygenated hemoglobin, and melanin), and these spectra depend on the concentrations of chromophores in skin tissue. Diffuse reflectance spectroscopy has been widely used for the evaluation of human skin chromophores at a single location.[1–10] The multispectral imaging technique is a useful tool for extending diffuse reflectance spectroscopy to spatial mapping of the chromophores in skin tissue. This can be simply achieved by a monochromatic CCD camera with narrow band filters and a white light source, which has been used to investigate the hemoglobin perfusion in living tissue.[11–13]

In clinical conditions, simpler, more cost-effective, and more portable equipment is needed. The digital RGB imaging technique is a promising tool for satisfying these demands for practical application. Imaging with broadband filters, as in the case of digital RGB imaging, can also provide spectral images without mechanical rotation of a filter wheel. Separated images of melanin and hemoglobin concentrations have been extracted from the RGB digital image with the aid of independent component analysis for the diffuse reflectance spectra of human skin.[14] An approach[15,16] has been developed for visualizing the concentration of red blood cells in the subsurface microcirculation of skin tissue. Using differences in the wavelength dependence of the absorption spectra between hemoglobin and background tissue, a tissue viability index, which is defined as a global expression of the capacity of the tissue to react to stimuli by altering microvascular perfusion, is evaluated based on the RGB values. In order to map the melanin, total hemoglobin, and oxygen saturation in human skin, RGB digital images of human skin were analyzed based on principal component analysis.[17] In this method, the RGB values are converted into three scores for the principal components of the reflectance spectra by the first look-up table. These three scores are then converted to the concentrations of melanin, total hemoglobin, and oxygen saturation, by the second look-up table.

We previously proposed a method by which to visualize the concentrations of melanin, oxygenated blood, and deoxygenated blood distributed in the skin tissue using a digital RGB image.[18] In this method, the RGB values are converted into the tristimulus values in the Commission Internationale de l'Éclairage XYZ (CIEXYZ) color space, which is compatible with the common RGB working space of the National Television Standards Committee (NTSC), the standard RGB (sRGB), etc. A Monte Carlo

Address all correspondence to: Izumi Nishidate, Tokyo University of Agriculture and Technology, Graduate School of Bioapplications and Systems Engineering, 2-24-16, Naka-cho, Koganei, Tokyo 184-8588 Japan; Tel: 81-42-388-7065; Fax: 81-42-388-7065; E-mail: inishi@cc.tuat.ac.jp

simulation (MCS) of light transport for the human skin model is used to specify the relationship among the tristimulus *XYZ* values and the concentrations of melanin, oxygenated blood, and deoxygenated blood. Images of total blood concentration and oxygen saturation can also be reconstructed from the results of oxygenated blood and deoxygenated blood. In the present study, we further investigate the validity of the proposed method for visualizing the hemodynamics of human skin tissue. Experiments using tissue-like agar gel phantoms are conducted in order to simulate the transition from oxygenated blood to deoxygenated blood in dermis *in vitro*. In order to confirm the applicability of the method to evaluate human skin hemodynamics, *in vivo* imaging of the total blood concentrations and tissue oxygen saturation are performed for 14 subjects during upper limb occlusion at pressures of 50 and 250 mm Hg. The responses of blood flow to the occlusion are evaluated by the forearm volume changes measured by a conventional strain-gauge plethysmograph (SPG). The results of total blood concentration obtained by the proposed method are compared to the SPG recordings. The results of oxygen saturation are discussed based on the physiological perspectives for microcirculation in human skin tissue.

2 Principle

RGB values of a pixel on a skin surface image acquired by a digital camera can be expressed as

$$
\begin{bmatrix} R \\ G \\ B \end{bmatrix} = \mathbf{L_1} \begin{bmatrix} X \\ Y \\ Z \end{bmatrix},
\tag{1}
$$

where *X*, *Y*, and *Z* are tristimulus values in the CIEXYZ color system and are defined as

$$
X = k \sum E(\lambda) \bar{x}(\lambda) O(\lambda),
\tag{2}
$$

$$
Y = k \sum E(\lambda) \bar{y}(\lambda) O(\lambda),
\tag{3}
$$

$$
Z = k \sum E(\lambda) \bar{z}(\lambda) O(\lambda).
\tag{4}
$$

and $\mathbf{L_1}$ is a transformation matrix to convert *XYZ* values to the corresponding RGB values and exists for each working space (NTSC, PAL/SECAM, sRGB, etc.). In addition, λ, $E(\lambda)$, and $O(\lambda)$ are the wavelength, the spectral distribution of the illuminant, and the diffuse reflectance spectrum of human skin, respectively, and $\bar{x}(\lambda)$, $\bar{y}(\lambda)$, and $\bar{z}(\lambda)$ are color matching functions in the CIEXYZ color system. The value of constant *k* that results in *Y* being equal to 100 for the perfect diffuser is given by

$$
k = 100 \Big/ \sum E(\lambda) \bar{y}(\lambda).
\tag{5}
$$

In Eqs. (2)–(5), the summation can be carried out using data at 10 nm intervals, from 400 to 700 nm. Assuming that the skin tissue consists primarily of the stratum corneum, epidermis containing melanin, and dermis containing oxygenated and deoxygenated blood, the diffuse reflectance of skin tissue *O* can be expressed as:

$$
O = I/I_0 = \left[\int_0^\infty P_{sc}(\mu_{s,sc}, g_{sc}, l_{sc}) \exp(-\mu_{a,sc}l_{sc})dl_{sc} \right]
$$
$$
\times \left[\int_0^\infty P_e(\mu_{s,e}, g_e, l_e) \exp(-\mu_{a,m}l_e)dl_e \right]
$$
$$
\times \left\{ \int_0^\infty P_d(\mu_{s,d}, g_d, l_d) \exp[-(\mu_{a,ob} + \mu_{a,db})l_d]dl_d \right\},
\tag{6}
$$

where I_0 and I are the incident and detected light intensities, respectively, $P(\mu_s, g, l)$ is the path length probability function that depends on the scattering properties, as well as on the geometry of the measurements, μ_s, μ_a, g, and l are the scattering coefficient, the absorption coefficient, the anisotropy factor, and the photon path length, respectively. In addition, the subscripts *m*, *ob*, *db*, *sc*, *e*, and *d* indicate melanin oxygenated blood, deoxygenated blood, the stratum corneum, epidermis, and dermis, respectively. The absorption coefficient of each chromophore is expressed as the product of its concentration *C* and extinction coefficient ε, i.e., $\mu_a = C\varepsilon$. Therefore, the RGB values are expressed as functions of C_m, C_{ob}, and C_{db}.

Figure 1 shows the flow of estimation using the proposed method. First, RGB values in each pixel of the image are transformed into *XYZ* values by a matrix $\mathbf{N_1}$ as

$$
\begin{bmatrix} X \\ Y \\ Z \end{bmatrix} = \mathbf{N_1} \begin{bmatrix} R \\ G \\ B \end{bmatrix}.
\tag{7}
$$

We determined the matrix $\mathbf{N_1}$ based on measurements of a standard color chart (ColorChecker, X-Rite Incorporated, Michigan) that has 24 color chips and is supplied with data giving the CIEXYZ values for each chip under specific illuminations and corresponding reflectance spectra. The values of *X*, *Y*, and *Z* are then transformed into C_m, C_{ob}, and C_{db} by a matrix $\mathbf{N_2}$. It is difficult to determine the matrix $\mathbf{N_2}$ based on $\mathbf{L_1}$ and Eqs. (2)–(6) because $P(\mu_s, g, l)$ and *l* for each layer are usually unknown. We calculated 300 diffuse reflectance spectra $O(\lambda)$ in a wavelength range from 400 to 700 nm at intervals of 10 nm by MCS for light transport[19] in skin tissue. We used the skin baseline absorption coefficient[20] as that of the stratum corneum. The absorption coefficient of the epidermis depends on the volume concentration of melanin in the epidermis C_m. We used the absorption coefficient of melanosome given in the literature[21] as the absorption coefficient of melanin $\mu_{a,m}$. This corresponds to the absorption coefficient of the epidermis for the case in which $C_m = 100\%$. Then, we derived the absorption coefficients of the epidermis for 10 different lower concentrations of $C_m = 1\%$ to 10% at intervals of 1%, by simply proportioning it to that for $C_m = 100\%$, and the absorption coefficients were input to the epidermis. The sum of the absorption coefficient of oxygenated blood for C_{ob} and that of deoxygenated blood for C_{db} were considered for the dermis. This summation provides the total blood concentration $C_{tb} = C_{ob} + C_{db}$ and oxygen saturation $SO_{2\%} = (C_{ob}/C_{tb}) \times 100$. The absorption coefficients of blood having a 44% hematocrit with 150 g/l of hemoglobin[22] were assumed to be that of the dermis for the case in which $C_{tb} = 100\%$ and were input to the dermis as $\mu_{a,ob} + \mu_{a,db}$. Then, the absorption coefficients of the dermis were derived for 5 different concentrations
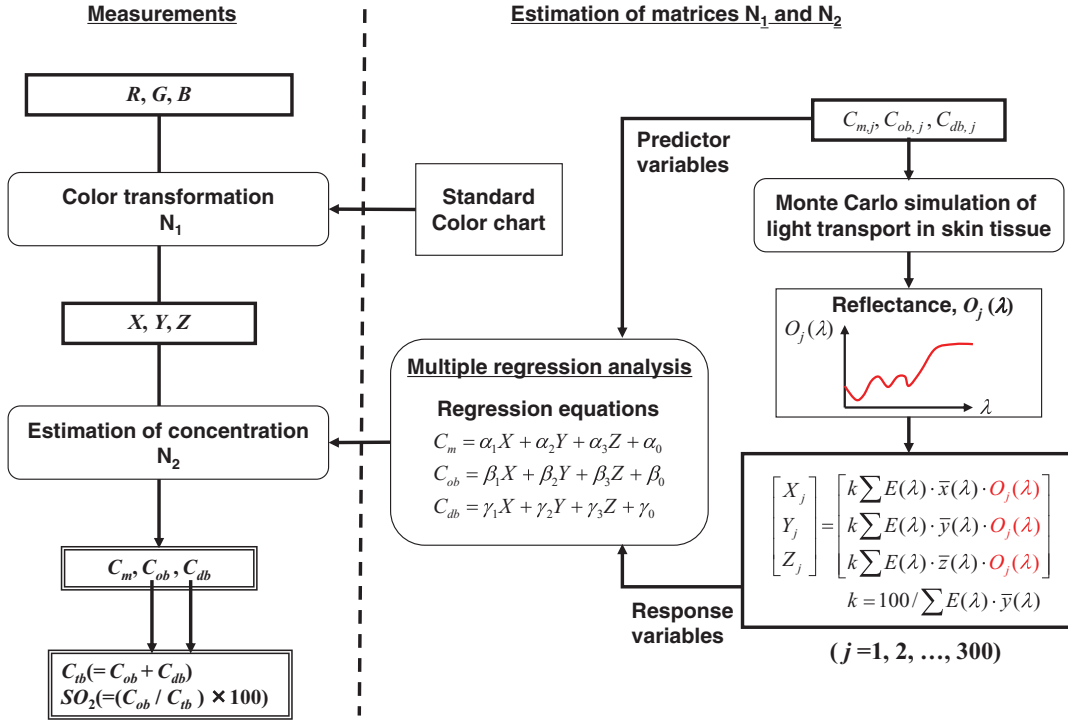
Measurements | **Estimation of matrices N$_1$ and N$_2$**

Fig. 1 Flow of the estimation process for C_m, C_{ob}, C_{db}, C_{tb}, and SO_2.

of $C_{tb} = 0.2$, 0.4, 0.6, 0.8, and 1.0% for six different cases of $SO_2 = 0$, 20, 40, 60, 80, and 100%. Typical published values for $\mu_s(\lambda)$[23] and $g(\lambda)$[24] were input to the stratum corneum, epidermis, and dermis, which are provided as a function of wavelength. The layer thicknesses of stratum corneum, epidermis, and dermis were set to be 0.02, 0.06, and 4.92 mm, respectively. The refractive index of the stratum corneum was set to be 1.47.[25] The refractive index of the epidermis was set to be 1.3725, which is the average value of the volar side of the lower arm, the granular layer of the palm of the hand, and the basal layer of the palm of the hand.[25] The refractive index of the dermis was set to be 1.42, which is the average value of the volar side of the lower arm and the palm of the hand.[25] The optical parameters used in the Monte Carlo simulation for the skin tissue model are summarized in Fig. 2. The XYZ-values were then calculated based on the simulated $O(\lambda)$. The above calculations were performed for various combinations of C_m, C_{ob}, and C_{db} in order to obtain the data sets of chromophore concentrations and XYZ-values. Multiple regression analysis with 300 data sets established three regression equations for C_m, C_{ob}, and C_{db}:

$$C_m = a_0 + a_1 X + a_2 Y + a_3 Z, \tag{8}$$

$$C_{ob} = b_0 + b_1 X + b_2 Y + b_3 Z, \tag{9}$$

$$C_{db} = c_0 + c_1 X + c_2 Y + c_3 Z. \tag{10}$$

The regression coefficients a_i, b_i, and c_i ($i = 0, 1, 2, 3$) reflect the contributions of the XYZ-values to C_m, C_{ob}, and C_{db}, respectively, and were used as the elements of a 4×3 matrix $\mathbf{N_2}$ as

$$\mathbf{N_2} = \begin{bmatrix} a_0 & a_1 & a_2 & a_3 \\ b_0 & b_1 & b_2 & b_3 \\ c_0 & c_1 & c_2 & c_3 \end{bmatrix}. \tag{11}$$

Transformation with $\mathbf{N_2}$ from the tristimulus values to the chromophore concentrations is thus expressed as

$$\begin{bmatrix} C_m \\ C_{ob} \\ C_{db} \end{bmatrix} = \mathbf{N_2} \begin{bmatrix} 1 \\ X \\ Y \\ Z \end{bmatrix}. \tag{12}$$
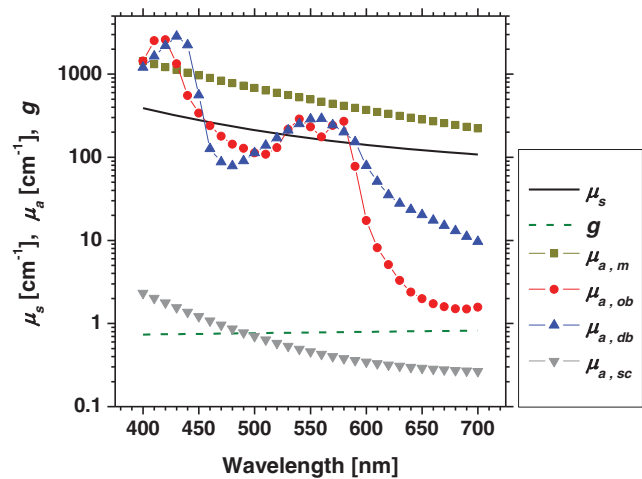

Fig. 2 Optical parameters used in the Monte Carlo simulation for the skin tissue model. The absorption coefficients of skin baseline (from Ref. 20) was used as those of the stratum corneum $\mu_{a,\,sc}$. The absorption coefficients for melanin in epidermis $\mu_{a,\,m}$ (from Ref. 21); oxygenated blood in dermis $\mu_{a,\,ob}$ (from Ref. 22); deoxygenated blood in dermis $\mu_{a,\,db}$ (from Ref. 22). The scattering coefficients μ_s (from Ref. 23) and g (from Ref. 24) was used for stratum corneum, epidermis, and dermis.
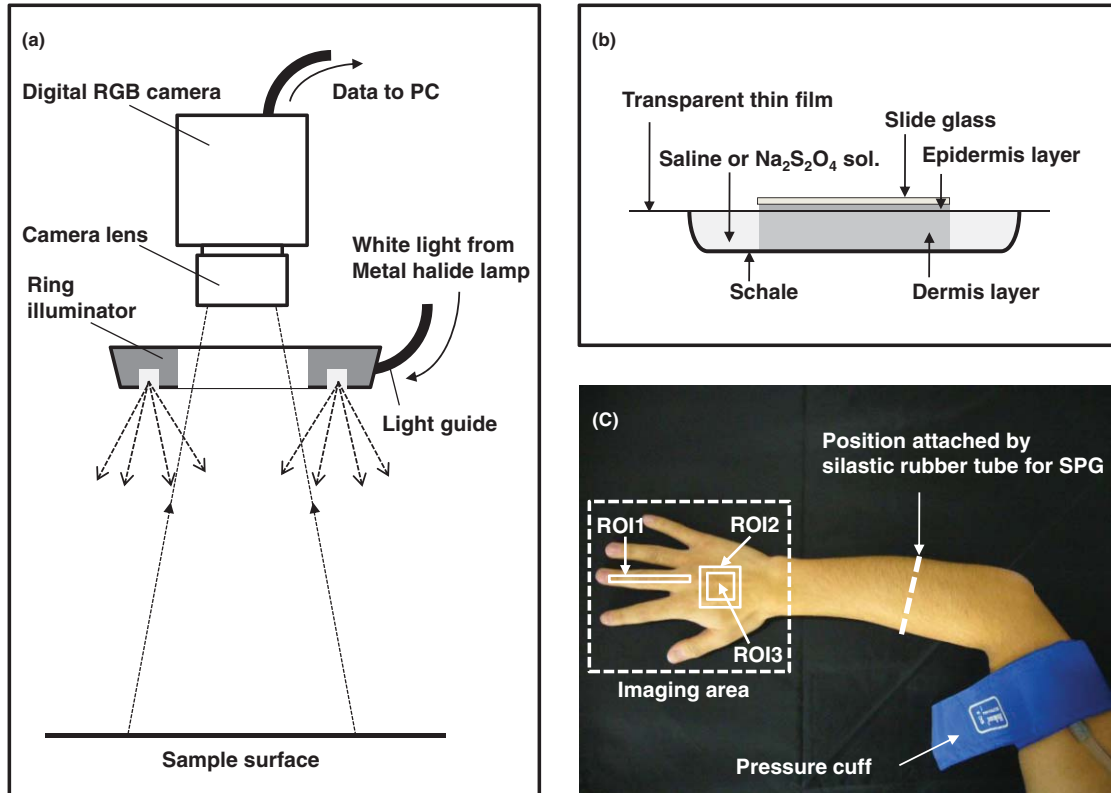
Fig. 3 Experimental configurations of (a) the imaging system, (b) the tissue-like agar gel phantom, and (c) the *in vivo* experiments with upper arm occlusion.

The computation times for the Monte Carlo simulation on obtaining all the simulated spectra and the matrix N_2 in Eq. (11) were 9.2 h and 10 s, respectively. Once we determine the matrices N_1 and N_2, images of C_m, C_{ob}, and C_{db} are reconstructed without the MCS. The total blood concentration image is simply calculated as $C_{tb} = C_{ob} + C_{db}$. The oxygen saturation image can also be reconstructed as $SO_2\% = (C_{ob}/C_{tb}) \times 100$.

3 Materials and Method

3.1 *Measurement Apparatus*

Figure 3 schematically shows the experimental configurations for (a) the imaging system, (b) the tissue-like agar gel phantom, and (c) *in vivo* experiments with upper arm occlusion. A metal halide lamplight (LA-180Me-R, Hayashi, Japan) illuminated the surface of a sample via a light guide with a ring illuminator. The light source covered a range from 380 to 740 nm. Diffusely reflected light was captured by a 24-bit RGB CCD camera (DFK-21BF04, Imaging Source LLC, USA) with a camera lens (Pentax/Cosmica, Japan; f 16 mm, 1:1.4) to acquire an RGB color image of 640 × 480 pixels. The field of view of the imaging system was 360 mm × 270 mm. The lateral resolution of the images was estimated to be 0.56 mm. This means the best resolution with a nonscattering object. An IR-cut filter in the camera rejects unnecessary longer-wavelength light (> 700 nm). A standard white diffuser with 99% reflectance (SRS-99-020, Labsphere Incorporated, New Hampshire) was used to correct instrument to instrument difference in output of the camera and the spatial nonuniformity of the illumination.

The RGB image was an average of 16 video frames and it was stored in a personal computer and analyzed according to the visualization process described above. The computation time for analyzing a typical human skin image was 5 s. RGB filters usually have cross-talk. The regression model used in the present study is based on the results of Monte Carlo simulation. We derived the theoretical diffuse reflectance spectra from the Monte Carlo simulation. A set of theoretical tristimulus values in the CIEXYZ color system, X, Y, and Z, were calculated using the diffuse reflectance spectrum, the spectral distribution of the illuminant, and color matching functions based on Eqs. (2)–(4). In this case, the color matching functions correspond to the product of the transmittance spectra of RGB color filters and the spectral sensitivity of the CCD. Like RGB filters, the color matching functions also have cross-talk. We derive RGB values from the theoretical XYZ values using the color transformation matrix L_1 in Eq. (1). Since this method estimates the values of C_m, C_{ob}, and C_{db} from the XYZ values, the regression model takes the cross-talk of RGB values into account in the estimation of these chromophore concentrations.

3.2 *Experiments Using Phantoms*

The tissue-like agar gel phantom used in the present study consists of an epidermis layer and a dermis layer. We prepared an agar solution by diluting agar powder (Ina Food Industrial Incorporated, Ina, Japan) with saline at a weight ratio of 0.8%. Intralipid 10% stock solution (Fresenius Kabi AB, Sweden) was added to the agar solution to cause scattering in the phantom.

The resultant solution was used as a base material for the epidermis and dermis layers. The final volume concentration of Intralipid in each layer was 1%. We tried to make the phantoms with three-layers similar to the theoretical skin model. However, it was difficult to make a thinned layer representing the stratum corneum by the agar gel in the present study. We investigated the effect of the stratum corneum layer on the RGB values numerically. We made a comparison between the RGB values calculated from the Monte Carlo skin model with and without the stratum corneum layer. The difference in the RGB value between the two models was 2.8 on average. This difference may be of minor importance for simulating the transition from oxygenated blood to deoxygenated blood in dermis. Thus, we ignored the stratum corneum layer in the phantom experiments. A coffee solution was introduced as a substitute for melanin into the base material, and this mixture was used to make the epidermis. Therefore, we used the variable C_c for the epidermis layer in the phantom experiments. Several materials, such as India ink, have been used to mimic the absorption properties of melanin.[26] We first tried to mimic the absorption spectrum using an India ink solution. We investigated the absorbance spectrum of India ink (R591217, Rotring, Germany) based on the transmittance measurement in the preliminary experiment. Figure 4 shows the measured absorption spectra of India ink solution and coffee solution. The absorption spectrum of melanin[21] is also presented in Fig. 4. The absorption spectrum of the India ink solution decays linearly as the wavelength increases, whereas that of melanin decays exponentially as the wavelength increases. Therefore, it was difficult to reproduce the diffuse reflectance spectra of human skin over the visible wavelength range using India ink. Thus, we used a coffee solution to mimic the absorption spectrum of melanin. The coffee solution contained a brown pigment called melanoidin.[27] The absorption spectrum of melanoidin[28,29] has been reported to be similar to that of melanin. We observed the absorbance spectrum of coffee solution within a cuvette based on transmittance measurements. As shown in Fig. 4, the absorption spectrum of
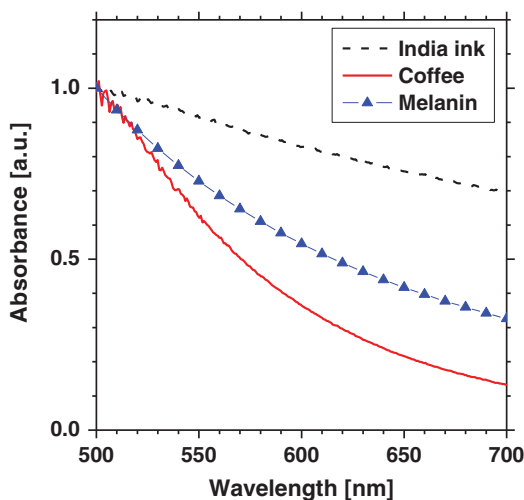
the coffee solution decays exponentially as the wavelength increases. An oxygenated dermis was made by adding a small amount of fully oxygenated horse blood having a 44% hematocrit to the base material. We established oxygenation of the horse blood by gassing it with 95% O_2, 5% CO_2.

The volume concentration of the coffee solution in the epidermis layer was set to be $C_c = 5.0\%$, whereas that of oxygenated blood in the dermis layer was set to be $C_{tb} = 0.4\%$. Therefore, the volume concentrations of deoxygenated blood and total blood and the oxygen saturation were assumed to be $C_{db} = 0.0\%$, $C_{tb} = 0.4\%$, and $SO_2 = 100\%$, respectively. All of these layers were hardened in various molds having the required thickness and size by cooling at approximately 5.5°C for 30 min. The thickness of the epidermis and dermis layers were made to be 1.0 and 5.0 mm, respectively, whereas the area of each layer was 26 mm × 23 mm. These layers were then stacked to obtain a layered phantom.

Empirical formulas for the phantom should also be prepared. The Monte Carlo simulations for the phantom conditions generated spectral diffuse reflectance samples ranging from 400 to 700 nm. The optical parameters of $\mu_s(\lambda)$ and $\mu_a(\lambda)$ for the phantom were determined by the inverse Monte Carlo method for measured diffuse reflectance and total transmittance.[8,30,31] Optical properties for the skin tissue phantoms estimated by the inverse Monte Carlo method are shown in Figure 5. The refractive index n for each layer was assumed to be 1.33 at three wavelengths. The anisotropy factor g of Intralipid was derived from the equation reported in literature[32] as,

$$g(\lambda) = 1.1 - 0.58 \times \lambda \times 10^{-3}, \quad (13)$$

where λ is in nanometers. We used it for the epidermis and dermis layers. In order to compensate for the difference in the thickness of the epidermis between the phantom and human skin, $\mu_s(\lambda)$ and $\mu_a(\lambda)$ were controlled so that $O(\lambda)$ of the phantom became close to that of the human skin by regulating the concentration of the Intralipid and coffee solution. The optical parameters for the phantom were reported previously.[8,30,31] Before measurement, the four sides of the dermis layer were surrounded with saline, as shown in Fig. 3(b). In order to simulate the transition from oxygenated blood to deoxygenated blood in
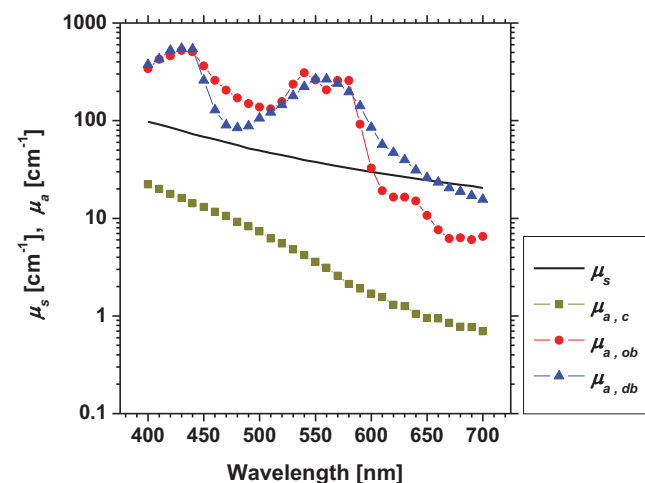

Fig. 4 Absorption spectra of India ink solution (dashed line) and coffee solution (solid line) obtained from the transmittance measurements, and absorption spectrum of melanin (from Ref. 21). All the absorption spectra are normalized at 500 nm.

Fig. 5 Optical properties for the skin tissue phantoms estimated by the inverse Monte Carlo method.

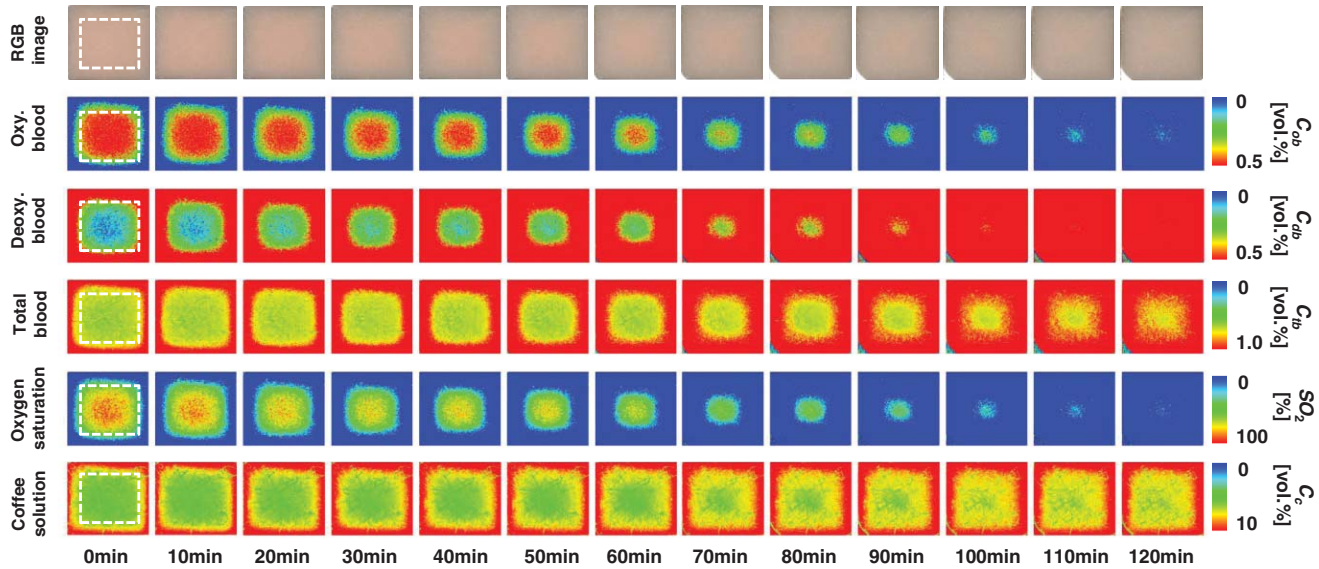**Fig. 6** Typical images obtained from a phantom, the dermis layer of which was immersed in $Na_2S_2O_4$-added saline (from top to bottom: RGB image, C_{ob}, C_{db}, C_{tb}, SO_2, and C_c) for different time points during measurement.

dermis *in vitro*, the saline surrounding the phantom was syringed out, and then a $Na_2S_2O_4$-added saline was injected after onset of the measurement. In order to avoid contact between the $Na_2S_2O_4$ and the upper face of the dermis layer and the epidermis layer, a transparent thin film having a thickness of 10 μm was introduced between the epidermis layer and the dermis layer. A slide glass on the epidermis layer was naturally coupled to the phantom by a drop of saline. The $Na_2S_2O_4$-added saline was applied to the phantoms for the three samples under the same conditions.

The proposed method assumes that the scattering coefficients $\mu_s(\lambda)$ and the thickness t of the skin tissue are known, and typical values reported in the literature are used to derive the empirical formulas. However, these values have subject-to-subject variability and may change due to the physiological or structural condition of the tissue. In order to investigate the effect of variation in scattering coefficients and thickness of the epidermis on the measurements, we also performed experiments on the phantoms for various values of $\mu_s(\lambda)$ and t. For test samples, the values of $\mu_s(\lambda)$ in the epidermis layer were set with a 50% decre-

ment or increment of the typical value, whereas those of t in the epidermis layer were set with a 50% decrement or increment.

3.3 Upper Arm Occlusion Experiments

A pressure cuff was applied to the upper arms of 14 Japanese subjects (10 males and four females, mean age: 25 ± 8 yr), as shown in Fig. 3(c). A SPG (EC6, D.E. Hokanson, Washington) and a rapid cuff inflator (E-20, D.E. Hokanson, Washington) were used to measure *in vivo* forearm volume change $\Delta V/V$ ml/100 ml, which has been used to evaluate limb blood flow.[33,34] The SPG is a device that measures the volume changes in limbs and digits using a gauge consisting of a mercury-filled silastic rubber tube. The volume change of tissue induced by the blood flow causes the gauge to stretch or contract. The SPG can determine the volume change based on the variation of electrical resistance caused by the stretching or contraction of the gauge.[35] Measurements of limb blood flow at 50 mm Hg have been performed in order to estimate physiological indices of blood circulation such as arterial inflow rate, venous capacitance, and maximum venous outflow,[35] whereas those at 250
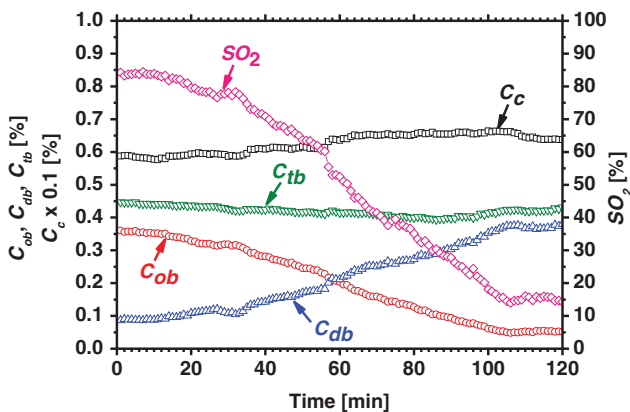

Fig. 7 Time courses of C_c, C_{ob}, C_{db}, C_{tb}, and SO_2 averaged over the ROIs (white squares) in Fig. 6.

Table 1 Relative errors of C_c, C_{ob}, C_{db}, C_{tb}, and SO_2 for different variations in $\mu_s(\lambda)$ and t of the epidermis layer for the phantom.

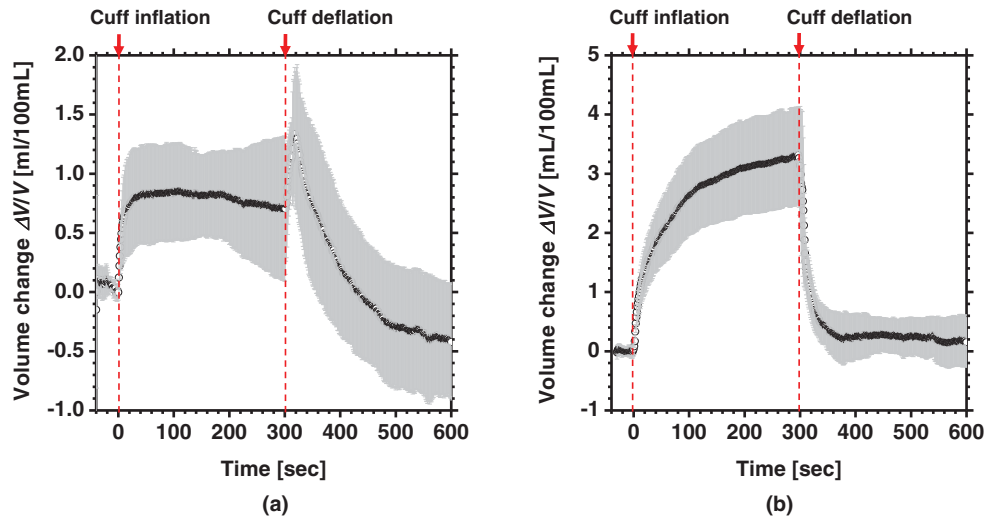|	Variation % from typical value	Relative error %				
		C_c	C_{ob}	C_{db}	C_{tb}	SO_2
$\mu_s(\lambda)$	-50	50	30	87	44	-11
	50	-21	-16	-35	-21	6
t	-50	-43	106	-14	77	15
	50	25	-51	108	-12	-44

Fig. 8 Time courses of forearm volume changes $\Delta V/V$ measured by SPG during upper arm occlusion at (a) 250 mm Hg and (b) 50 mm Hg. The error bars show the standard deviations ($n = 14$).

mm Hg have been performed to investigate the relationship between vasodilatation response and endothelial functions for a peripheral blood vessel.[34,35]

During the measurements, the subjects sat with their hands placed on a sample stage at approximately heart-level. After resting for 300 s, image acquisition and SPG recording were started and continued for 640 s at 4 s intervals. After 40 s of control, the cuff was inflated to 50 or 250 mm Hg for 300 s by

a rapid cuff inflator, which was then deflated for 300 s. Inflation of the cuff to 50 mm Hg prevents blood flow from leaving the measurement site but does not hinder arterial inflow, whereas that at 250 mm Hg blocks both venous outflow and the arterial inflow. Analyses of the RGB images and the forearm volume change $\Delta V/V$ were performed offline after the measurements were completed. Three regions of interest (ROIs) of different sizes were placed in different parts of each image, as shown in
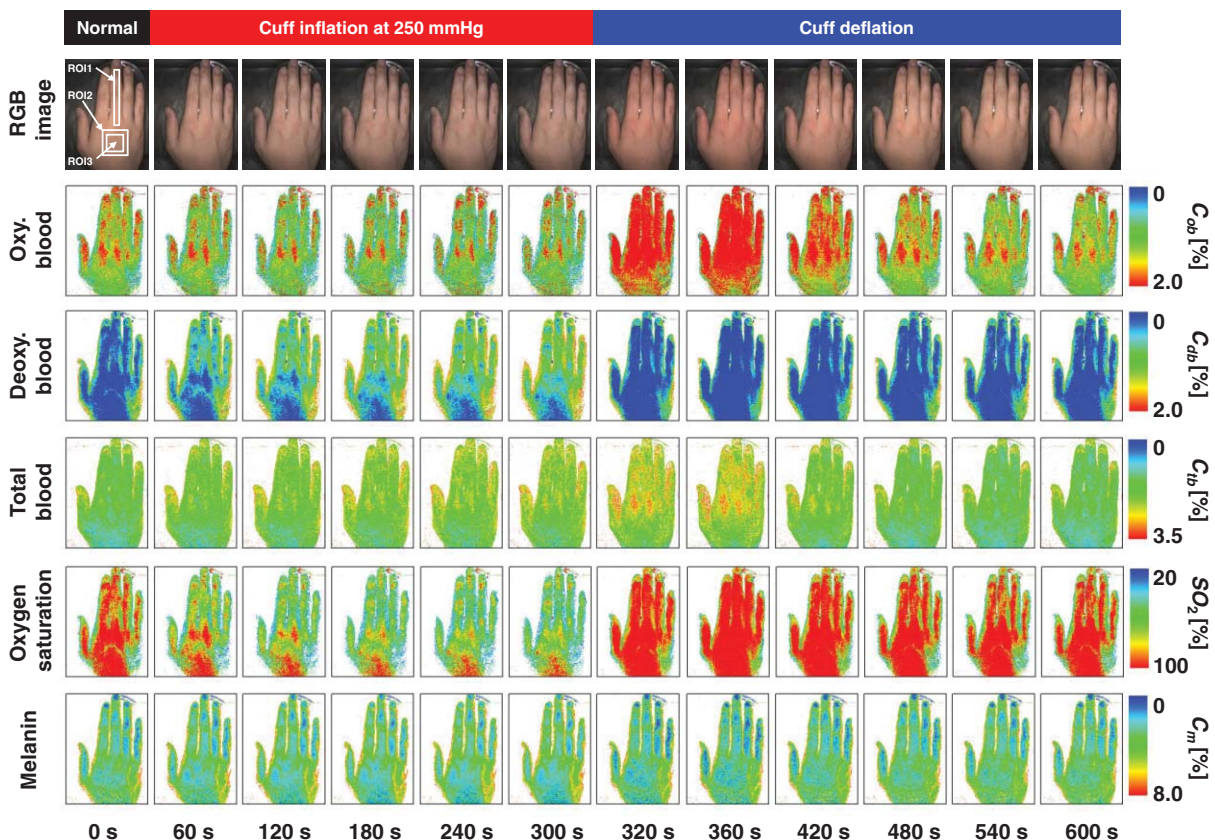

Fig. 9 Typical images of *in vivo* measurements during cuff occlusion at 250 mm Hg (from top to bottom: RGB image, C_{ob}, C_{db}, C_{tb}, SO_2, and C_m).
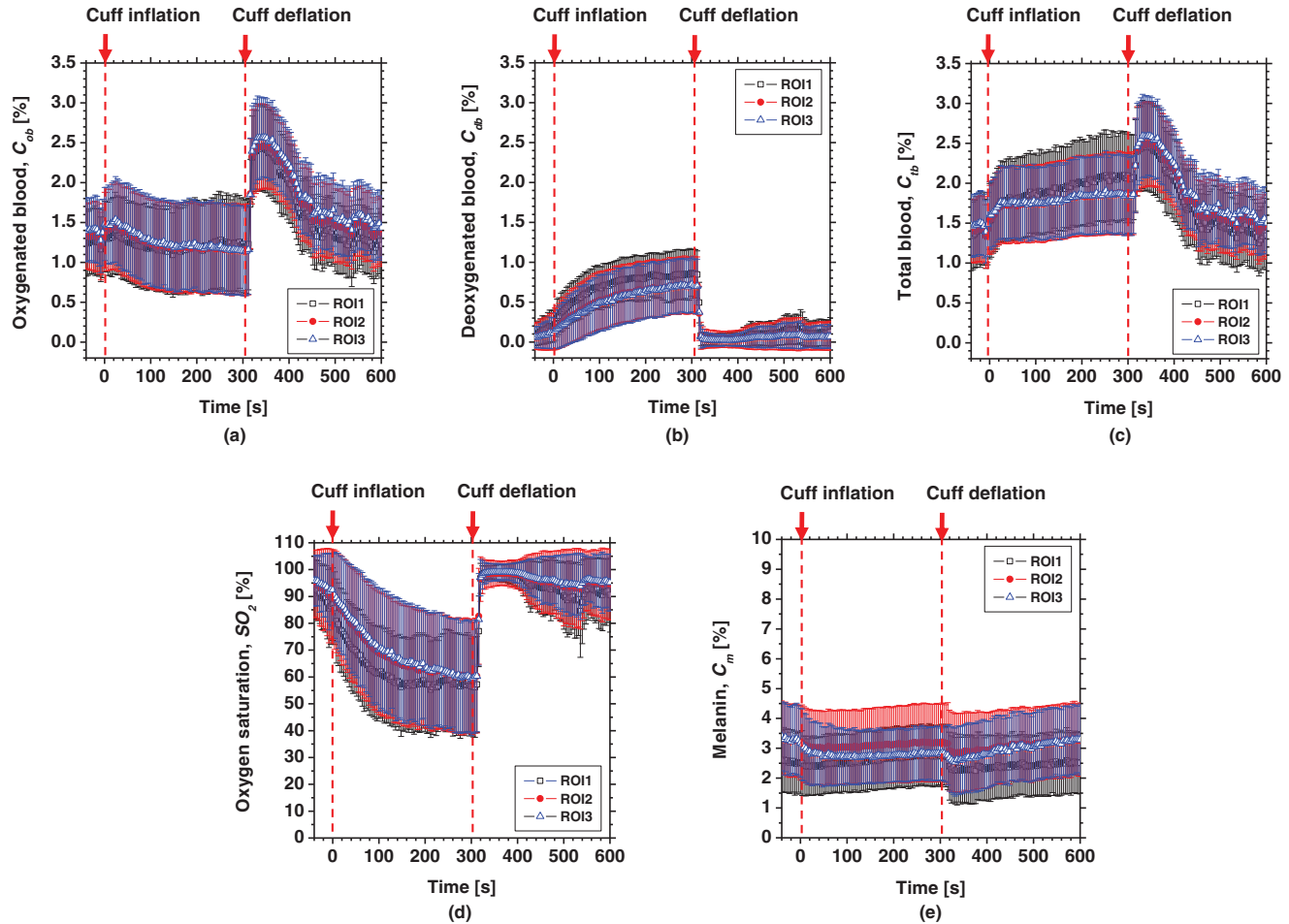
Fig. 10 Time courses averaged over the ROIs (white squares) in Fig. 9 of (a) oxygenated blood C_{ob}, (b) deoxygenated blood C_{db}, (c) total blood C_{tb}, (d) oxygen saturation SO_2, and (e) melanin C_m. The error bars show the standard deviations for each ROI.

Figure 3(c). The sizes of ROI1, ROI2, and ROI3 were 250×25 pixels, 150×150 pixels, and 100×100 pixels, respectively.

4 Results and Discussion

4.1 *Experiments Using Phantoms*

Figure 6 shows typical images obtained from a phantom, four sides of the dermis layer of which were immersed in $Na_2S_2O_4$-added saline, at different time points during the measurement. Note that the edge of the RGB image is dark before the application of $Na_2S_2O_4$ (0 min). This is primarily due to the light being less diffusive at the edge than in the center. Similar artifacts were also observed in the estimated images of C_c, C_{ob}, C_{db}, C_{tb}, and SO_2 Therefore, the results for the ROIs (white squares) in the images are discussed here. A correction map based on the spatial distribution of diffuse reflected light intensity from the phantom may be promising to correct for the edge effects. This issue should be investigated in a future work. The images of C_{db} and C_{ob} altered inversely from the edge to the center because only the sides of the phantom were surrounded by $Na_2S_2O_4$-added saline. Consequently, the reduction in SO_2 covered most of the image at the end of measurement ($t = 90$ min). The images of C_{tb} and C_c remained approximately constant because they are independent of the oxygen state of hemoglobin. The time courses of the average values over ROIs in the images of C_c, C_{ob}, C_{db}, C_{tb}, and SO_2 shown in Fig. 6 are plotted in Fig. 7. At the beginning of measurement, the values of C_c, C_{ob}, C_{db}, C_{tb}, and SO_2 were estimated to be $5.8 \pm 2.7\%$, $0.36 \pm 0.07\%$, $0.09 \pm 0.01\%$, $0.45 \pm 0.16\%$, and $84 \pm 19\%$, whereas the given values were 5.0%, 0.4%, 0.0%, 4.0%, and 100%, respectively. During measurement, C_{ob} decreased and C_{db} increased, whereas C_{tb} and C_c were almost unchanged, as should be expected. The value of SO_2 decreased gradually and finally fell to approximately 15%. The results obtained from the phantom experiment demonstrate the usefulness of the method in visualizing quantitatively the transition from oxygenated blood to deoxygenated blood in the dermis.

Table 1 lists the relative errors in C_c, C_{ob}, C_{db}, C_{tb}, and SO_2 for two different variations in $\mu_s(\lambda)$ and t of the epidermis layer. The estimated values of C_c, C_{ob}, C_{db}, and C_{tb} decrease as the variation in $\mu_s(\lambda)$ changes from negative to positive. This is because the absorption by each chromophore is estimated to be small due to the increase in $O(\lambda)$ associated with the increase in $\mu_s(\lambda)$. The estimated value of C_c decreases as the variation in t changes from positive to negative, whereas that of SO_2 increases. This is due to the following consideration. As the thickness of the epidermis layer becomes small, the probability that light is absorbed in it will decrease. Thus, the value of C_c will be underestimated if the thickness of the epidermis is
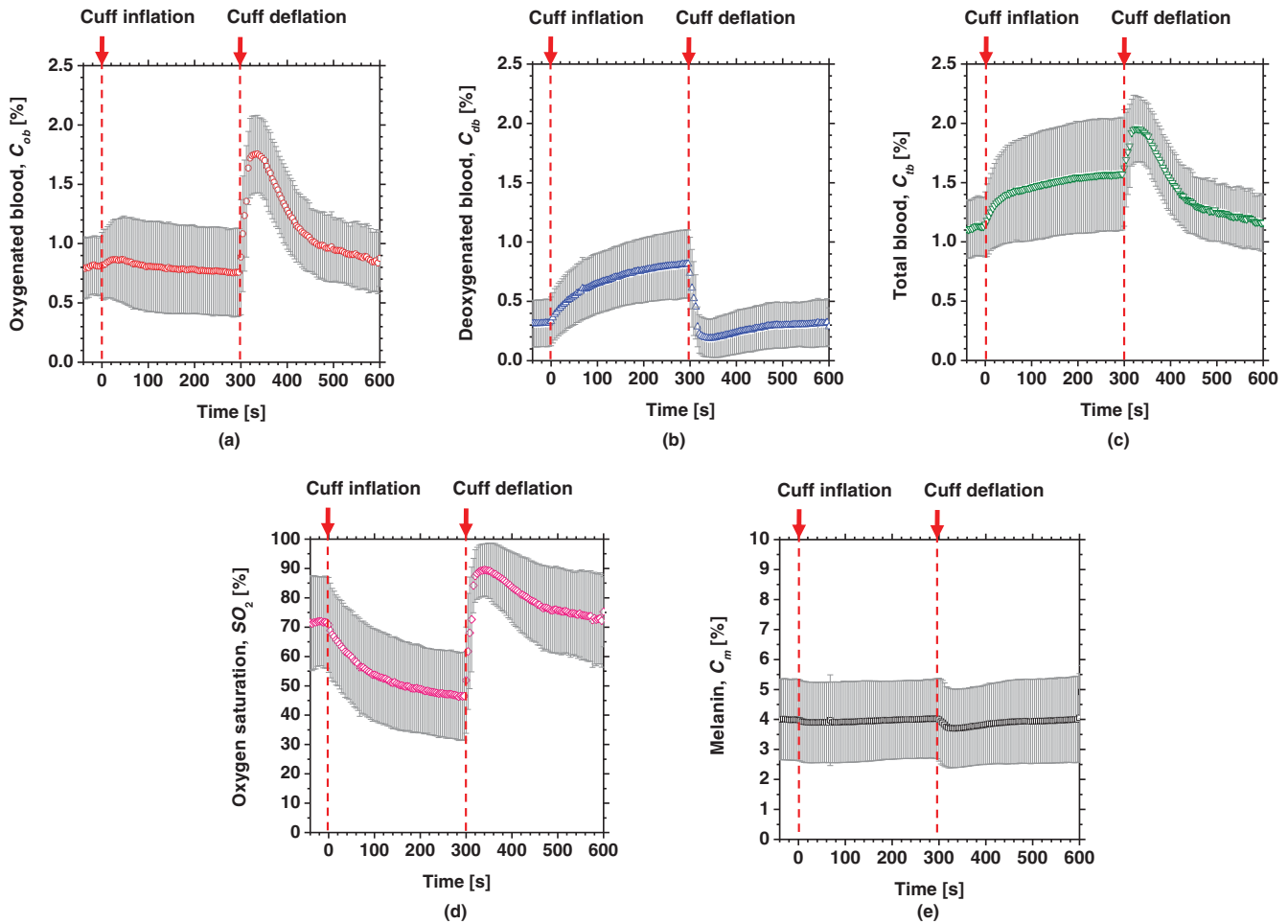
Fig. 11 Time courses of (a) C_{ob}, (b) C_{db}, (c) C_{tb}, (d) SO_2, and (e) C_m averaged over the three ROIs for all 14 subjects during cuff occlusion at 250 mm Hg. The error bars show the standard deviations ($n = 14$).

smaller than the typical value. On the other hand, more light will penetrate into the dermis layer as the epidermis layer becomes thinner. In this case, the diffuse reflectance will be affected by the absorption of hemoglobin in the dermis layer more strongly than that of the coffee solution in the epidermis. In addition, the hemoglobin strongly absorbs the light at the shorter wavelength. Therefore, the increase in diffuse reflectance at the longer wavelength is larger than that at the shorter wavelength. This may cause over- and underestimation of C_{ob} and C_{db}, respectively. Consequently, the oxygen saturation SO_2 will be overestimated if the thickness of the epidermis is smaller than the typical value.

4.2 *Upper Arm Occlusion Experiments*

Figure 8 shows the forearm volume change $\Delta V/V$ measured by the SPG for cuff pressures of (a) 250 mm Hg and (b) 50 mm Hg. In Fig. 8(a), $\Delta V/V$ first increases as a result of cuff inflation. A second increase due to reactive hyperemia is evident after cuff deflation. In Fig. 8(b), $\Delta V/V$ rises quickly after the inflation of the cuff, and the rate of increase in $\Delta V/V$ then slows. A rapid decrease in $\Delta V/V$ occurred after deflation of the cuff. Figure 9 shows an example of the *in vivo* results obtained from one single subject during cuff occlusion at 250 mm Hg. The time courses of C_m, C_{ob}, C_{db}, C_{tb}, and SO_2 averaged over the area

for the ROIs (white squares) in Fig. 9 are shown in Figs. 10(a)–10(e). Figure 11 shows the time courses of C_m, C_{ob}, C_{db}, C_{tb}, and SO_2 averaged over the three ROIs for all 14 subjects during cuff occlusion at 250 mm Hg. The average values of C_m and C_{tb} were $4.3 \pm 1.2\%$ and $1.1 \pm 0.4\%$, respectively, in pre-occlusion (control), which are close to typical values reported in the literature.[2,11,13] The average value of $71 \pm 16\%$ for SO_2 in pre-occlusion is lower than typical arterial SO_2, which ranges from 90% to 98%. Typical value of venous SO_2 is almost 60%. The value of SO_2 measured by this method represents oxygen saturation for the mixture of arterio-venous blood. Almost 75% of the total blood volume in whole body is contained within the veins and venules, whereas 25% of it is contained within the arteries and arterioles. Assuming that the blood volume ratio of venules and arterioles in the skin tissue is similar to that of whole body, and the oxygen saturation of arterial blood under the normal condition is 96%, the oxygen saturation of skin tissue is calculated to be 69%. This value is close to the average values of $71 \pm 16\%$ for SO_2 obtained by this method in preocclusion. During cuff occlusion, C_{ob} and C_{db} decreased and increased, respectively. The value of SO_2 exhibited the well-known deoxygenation curve, in which the oxygen saturation falls exponentially. The slight increase in C_{tb} probably has a physiological cause. This is because, during occlusion, the venous outflow is reduced more than the arterial inflow. This is supported by the results
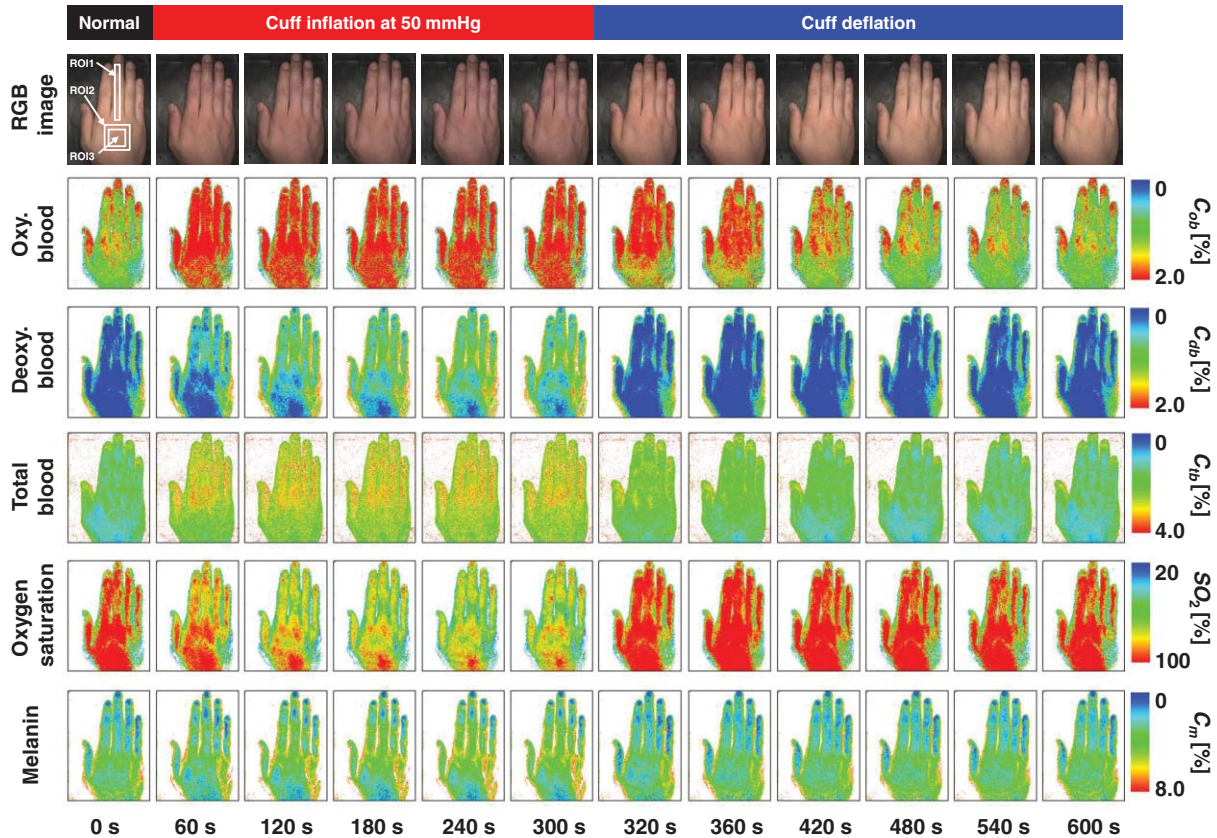
Fig. 12 Typical images of *in vivo* measurements during cuff occlusion at 50 mm Hg (from top to bottom: RGB image, C_{ob}, C_{db}, C_{tb}, SO_2, and C_m).

for $\Delta V/V$ shown in Fig. 8(a). After the cuff was deflated, both SO_2 and C_{tb} increased sharply and then gradually returned to their normal levels. The error ranges for each subject were taken into account for the calculation of the error range for the trace in Fig. 11. Therefore, interindividual differences in response times and levels may have caused some skewing of traces in Fig. 11.

Figure 12 shows an example of *in vivo* results obtained from one single subject during cuff occlusion at 50 mm Hg. The time courses of C_m, C_{ob}, C_{db}, C_{tb}, and SO_2 averaged over the ROIs (white squares) in Fig. 12 are shown in Figs. 13(a) through 13(e). Figure 14 shows the time courses of C_m, C_{ob}, C_{db}, C_{tb}, and SO_2 averaged over the three ROIs for all 14 subjects during cuff occlusion at 50 mm Hg. The first increase in C_{ob} appeared after the cuff was inflated, which caused a temporal increase in SO_2, probably due to the blockage of venous outflow and the continuous arterial inflow. After peaking, C_{ob} became constant, whereas C_{db} increased during occlusion. These changes in C_{ob} and C_{db} indicate the decrease of the arterial inflow rate and the deoxygenation of hemoglobin resulting from the consumption of oxygen by the tissue, respectively. The rapid decreases in both C_{ob} and C_{db} immediately after the deflation of the cuff suggest the outflow of venous blood. The tendency of the response in C_{tb} to the upper arm occlusions at 50 mm Hg corresponds to the results for $\Delta V/V$ shown in Fig. 9(b). Note that, whereas C_{db} decreases monotonically, the change in C_{ob} after deflation of the cuff has three separate phases: an initial rapid decrease, a slight increase, and then a gradual decrease. This means that the reactive response of arterial blood can be caused by the occlusion at not only 250 mm Hg but also 50 mm Hg. However, the reactive

response at 50 mm Hg cannot be observed in the results for the total blood volume, i.e., C_{tb} and $\Delta V/V$, because the slight variation in C_{ob} was hidden by the change in deoxygenated blood that decreases dramatically. This indicates the possibility of using this method to evaluate the post-occlusion reactive hyperemia at a pressure of 50 mm Hg. Despite the remarkable changes in C_{ob}, C_{db}, C_{tb}, and SO_2, the value of C_m, which is independent of temporary hemodynamics, remained almost unchanged during the measurements, as shown in Figs. 11 and 14. The results shown in Figs. 10 and 13 demonstrate that the use of ROIs of different sizes and in different parts of the hand would not change the results significantly. Although there are a number of artifacts due to the shadow originating from the curved and irregular surfaces of the hand, the lateral distributions of C_m, C_{ob}, C_{db}, C_{tb}, and SO_2, and their responses to the occlusion were successfully visualized.

Figure 15 shows images obtained from a Japanese subject of the inner forearm skin including a freckle. A high melanin concentration is observed in the area of the freckle and the estimated values of oxygenated and deoxygenated blood are extremely low and high, respectively. The RGB values in high-melanin areas of freckles will be very small at very low resolution, and the conversion to *XYZ* color space could compound likely artifacts in measurement. In this case, the conversion from RGB color space to *XYZ* color space may cause misestimation of oxygenated and deoxygenated blood in the dermis. The results shown in Fig. 15 imply a limitation of the method in measuring the hemodynamics of people with darker skin colors. Experiments involving individuals of African or Indian descent should be performed in the future.
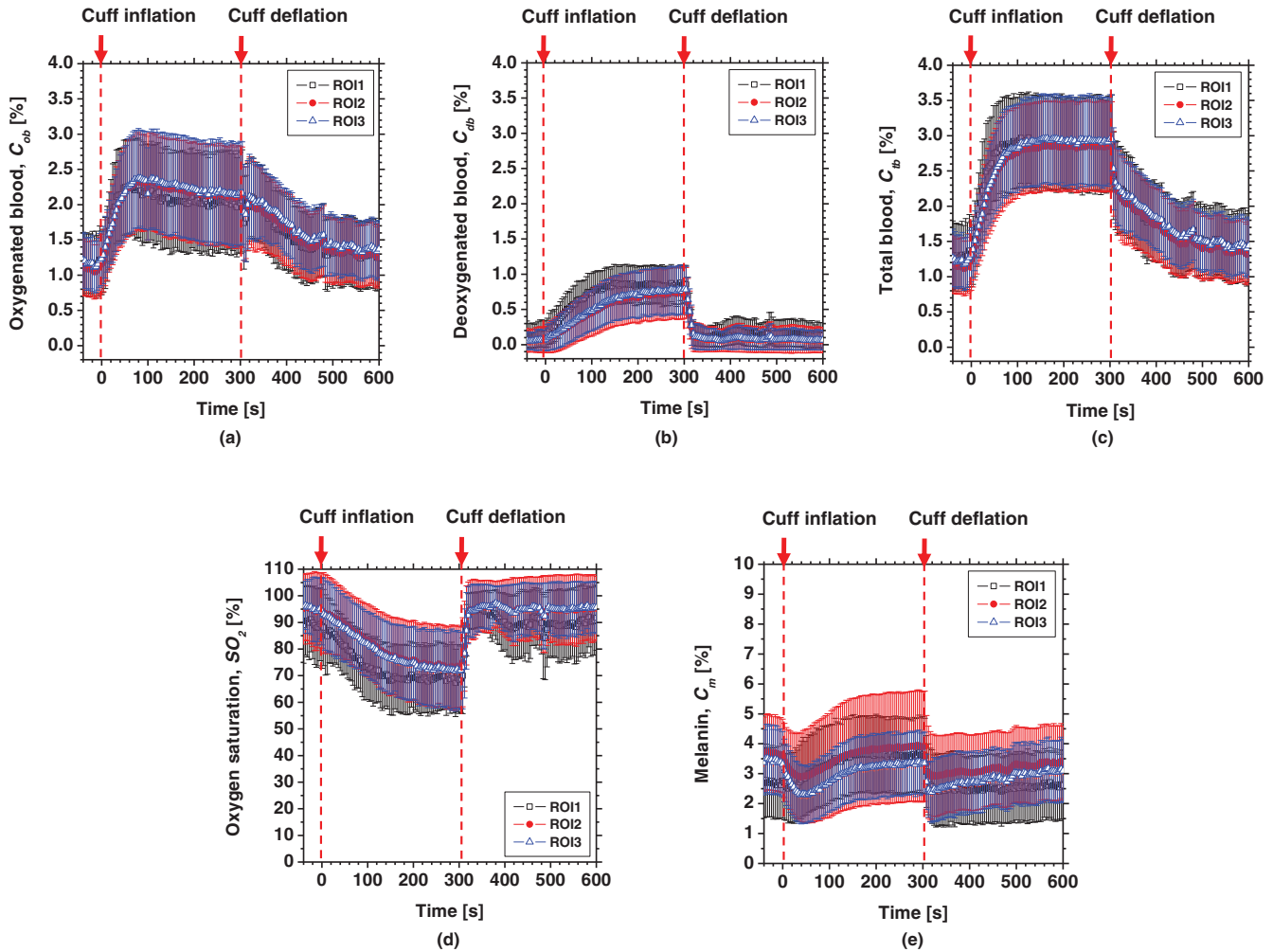
Fig. 13 Time courses averaged over the ROIs (white squares) in Fig. 12 of (a) oxygenated blood C_{ob}, (b) deoxygenated blood C_{db}, (c) total blood C_{tb}, (d) oxygen saturation SO_2, and (e) melanin C_m. The error bars show the standard deviations for each ROI.

We used a single thickness for the epidermis and the dermis and only one typical wavelength-dependent scattering value and anisotropy for skin in the Monte Carlo simulation to derive the regression Eqs. (8)–(10) for the concentration of melanin C_m, oxygenated blood C_{ob}, and deoxygenated blood C_{db}. We also assumed a single thickness for the epidermis and the dermis in the Monte Carlo simulation. As expected from the results of phantom experiments, changes in these parameters will affect the regression model. Diffusely reflected light from the skin will increase as the absorption of light in skin becomes small and will increase as the scattering coefficient $\mu_s(\lambda)$ becomes small. Thus, if the scattering coefficients $\mu_s(\lambda)$ of a sample are larger than the typical values used in the Monte Carlo simulation, the regression model will underestimate the chromophore concentrations. Diffusely reflected light from the skin will also increase as the anisotropy factors $g(\lambda)$ decrease. Therefore, if the anisotropy factors $g(\lambda)$ of a sample are larger than the typical values, the regression model will underestimate the chromophore concentrations. The probability that light is absorbed by melanin in the epidermis will be higher than the probability that light is absorbed by blood in the dermis as the epidermis becomes thicker. Therefore, if the thickness t of the epidermis is larger than the typical values, then the concentration of melanin in the epidermis

or that of blood may be under- or overestimated, respectively. Hence, the measurements could be varied with the changes in the scattering coefficients $\mu_s(\lambda)$, the anisotropy factors $g(\lambda)$, and the thickness t of each layer. However, the possibility of relative measurements of melanin, oxygenated blood, and deoxygenated blood in the skin tissue could still prove valuable. Studies on the Monte Carlo simulation model with the variations in the scattering coefficients, the anisotropy factors, and the thickness of each layer would strength the method in the future. We will investigate the matrix N_2 involving those variations further in future work.

This method should integrate all information along the depth direction because it relies on diffuse reflection. Therefore, the imaging system does not limit the depth of the measurement. The RGB camera used in the present study has a spectral sensitivity in the visible wavelength region from 400 to 700 nm. Light at longer wavelengths in this region may penetrate the subcutaneous region. Thus, the measurements shown in Figs. 9–14 in the original manuscript may reflect the hemodynamics not only of skin but also of the overall limb. This is supported by the fact that the time courses of C_{tb} shown in Figs. 9 through 14 correlate with the SPG reading, which measures the total blood flow primarily through skeletal muscle, skin, and bone. Cuff
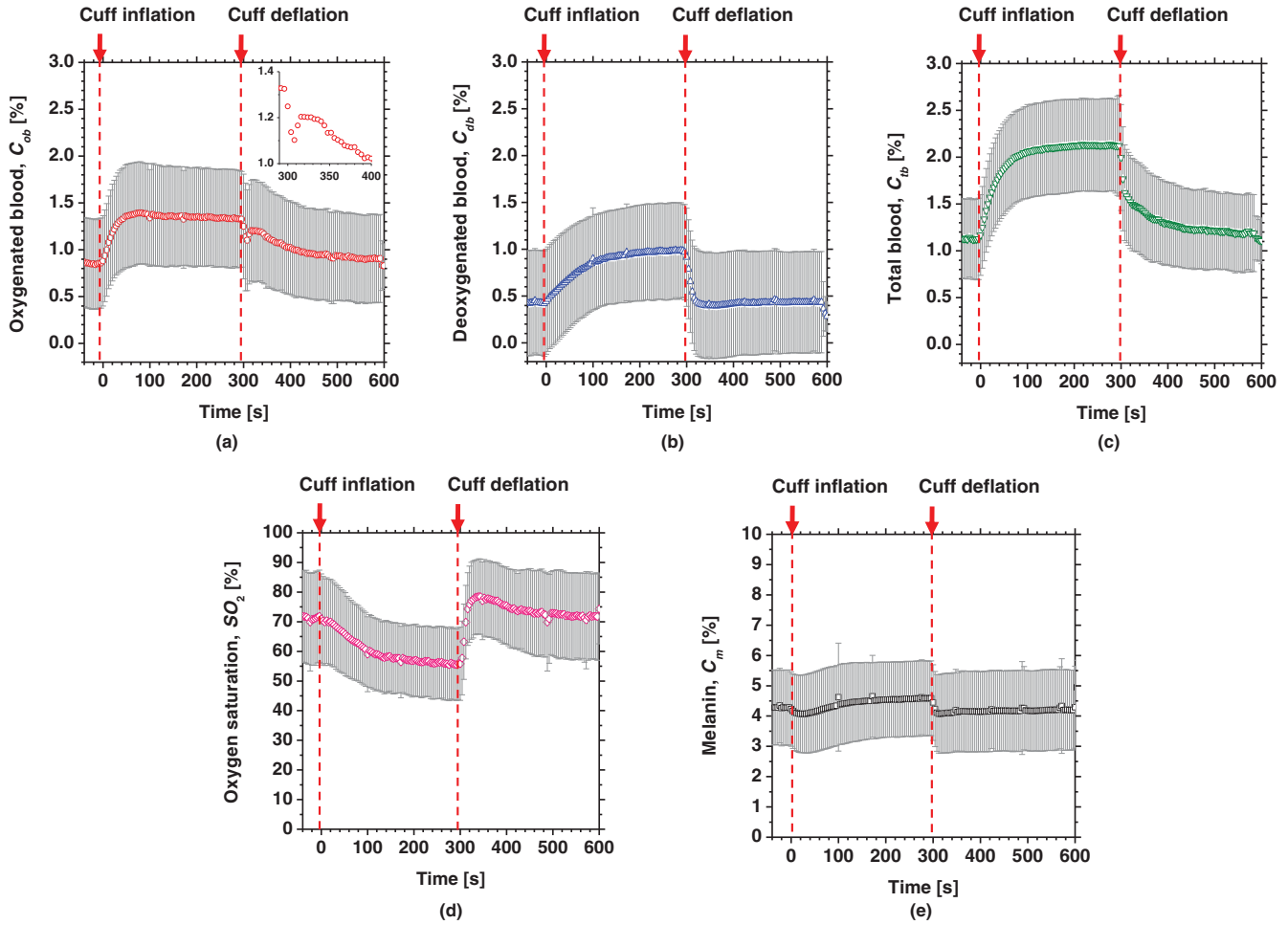
Fig. 14 Time courses of (a) C_{ob}, (b) C_{db}, (c) C_{tb}, (d) SO_2, and (e) C_m averaged over the three ROIs for all 14 subjects during cuff occlusion at 50 mm Hg. The error bars show the standard deviations ($n = 14$).
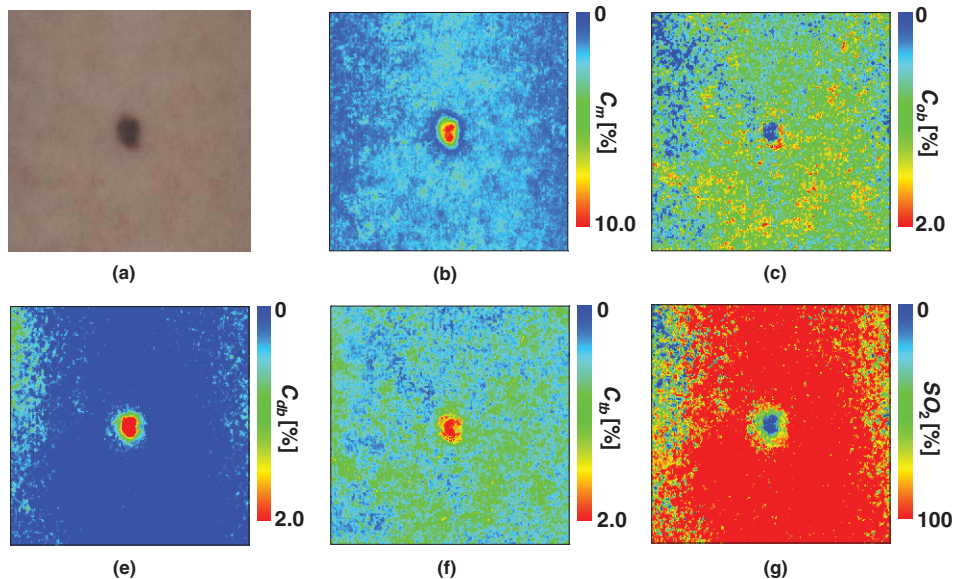

Fig. 15 Images of the inner forearm skin including a freckle obtained from a Japanese subject. (a) RGB image, (b) melanin C_m, (c) oxygenated blood C_{ob}, (d) deoxygenated blood C_{db}, (e) total blood C_{tb}, and (f) oxygen saturation SO_2.

pressures of 50 and 250 mm Hg used in the *in vivo* experiments should usually be higher than the venous blood pressures. Occlusions of the forearm with these pressures, therefore, may induce the onset of edema.[36–38] Edema will change the volume of the limb, thereby diluting the bulk concentration of the chromophores and some biological scatterers in the skin tissue. In such a case, under- or overestimation of C_m, C_{ob}, and C_{db} may have occurred due to the decrease in the bulk absorption or bulk scattering, respectively. The Monte Carlo simulated spectra in this study were noise-free, while the measured spectra always contain some noise in real applications. Since the matrix $\mathbf{N_2}$ is determined on the basis of the Monte Carlo simulated spectra, the estimated concentrations of chromophores can be affected by the noise. Although we performed the averaging procedure to reduce the noise component in the RGB image, the results presented in the manuscript may still have some errors due to the noise. It would be reasonable to add some noise in the Monte Carlo simulated spectra to simulate reality better and improve the robustness of the method. It may be helpful to apply partial least square (PLS) regression analysis instead of multiple regression analysis to obtain the matrix $\mathbf{N_2}$, because PLS regression analysis is particularly suited when the matrix of predictors has more variables than observations, and when there is multicollinarity among predictor variables. The imaging system used in the present study does not eliminate specular reflection from the measured reflected image. Thus, there should be some specular components in the measured RGB signals. On the other hand, we did not take the specular reflectance into account in the Monte Carlo simulation model. This specular component included in the measured RGB values could provide the estimation errors in C_m, C_{ob}, and C_{db}. The specular reflection may be eliminated by the use of the polarized imaging technique. These considerations should be investigated in the future.

5 Conclusion

In summary, we investigated a method that was specifically developed for visualizing concentrations of melanin, oxygenated blood, and deoxygenated blood distributed in skin tissue using RGB digital images. Monte Carlo simulation of light transport in the skin tissue specified a relation between the chromophore concentrations and RGB values. Images of total blood concentrations and oxygen saturation were also reconstructed. The feasibility of this method for monitoring the oxygenation state of blood in skin tissue was demonstrated through experiments using tissue-like agar gel phantoms. *In vivo* experiments confirmed the ability of the method to visualize the concentration of melanin, oxygenated blood, deoxygenated blood, total blood, and tissue oxygen saturation. The responses of the total blood concentration in the skin of the human hand acquired by this method as well as forearm volume changes obtained from the conventional SPG were comparable during upper arm occlusion at pressures of 50 and 250 mm Hg. The results of the present study demonstrate the possibility of visualizing the hemodynamics of subsurface skin tissue. The great advantages of this method are its simplicity and applicability, because the only devices required are a digital RGB camera with a known color profile, a white light source, and a personal computer. We expect to further extend this method in order to investigate the physiological and clinical indices of blood flow, such as the arterial inflow rate, the venous capacitance, and the maximum venous outflow.

References

1. J. B. Dawson, D. J. Barker, D. J. Ellis, E. Grassam, J. A. Cotterill, G. W. Fisher, and J. W. Feather, "A theoretical and experimental study of light absorption and scattering by *in vivo* skin," *Phys. Med. Biol.* **25**, 695–709 (1980).
2. J. W. Feather, M. H. -Saffar, G. Leslie, and J. B. Dawson, "A portable scanning reflectance spectrophotometer using visible wavelengths for the rapid measurement of skin pigments," *Phys. Med. Biol.* **34**, 807–820 (1989).
3. D. K. Harrison, S. D. Evans, N. C. Abbot, J. S. Beck, and P. T. McCollum, "Spectrophotometric measurements of haemoglobin saturation and concentration in skin during the tuberculin reaction in normal human subjects," *Clin. Phys. Physiol. Meas.* **13**, 349–363 (1992).
4. D. J. Newton, D. K. Harrison, C. J. Delaney, J. S. Beck, and P. T. McCollum, "Comparison of macro- and maicro-lightguide spectrophotometric measurements of microvascular haemoglobin oxygenation in the tuberculin reaction in normal human skin," *Physiol. Meas.* **15**, 115–128 (1994).
5. A. A. Stratonnikov and V. B. Loschenov, "Evaluation of blood oxygen saturation in vivo from diffuse reflectance spectra," *J. Biomed. Opt.* **6**, 457–467 (2001).
6. G. Zonios, J. Bykowski, and N. Kollias, "Skin melanin, hemoglobin, and light scattering properties can be quantitatively assessed in vivo using diffuse reflectance spectroscopy," *J. Invest. Dermatol.* **117**, 1452–1457 (2001).
7. G. N. Stamatas and N. Lollias, "Blood stasis contributions to the perception of skin pigmentation," *J. Biomed. Opt.* **9**, 315–322 (2004).
8. I. Nishidate, Y. Aizu, and H. Mishina, "Estimation of melanin and hemoglobin in skin tissue using multiple regression analysis aided by Monte Carlo simulation," *J. Biomed. Opt.* **9**, 700–710 (2004).
9. P. R. Bargo, S. A. Prahl, T. T. Goodell, R. A. Sleven, G. Koval, G. Blair, and S. L. Jacques, "*In vivo* determination of optical properties of normal and tumor tissue with white light reflectance and empirical light transport model during endoscopy," *J. Biomed. Opt.* **10**, 034018 (2005).
10. S.-H. Tseng, P. Bargo, A. Durkin, and N. Kollias, "Chromophore concentrations, absorption and scattering properties of human skin *in vivo*," *Opt. Express* **17**, 14599–14617 (2009).
11. M. G. Sowa, J. R. Payette, M. D. Hewko, and H. H. Mantsch, "Visible-near infrared multispectral imaging of the rat dorsal skin flap," *J. Biomed. Opt.* **4**, 474–481 (1999).
12. A. K. Dunn, A. Devor, H. Bolay, M. L. Andermann, M. A. Moskowitz, A. M. Dale, and D. A. Boas, "Simultaneous imaging of total cerebral hemoglobin concentration, oxygenation, and blood flow during functional activation," *Opt. Lett.* **28**, 28–30 (2003).
13. A. Vogel, V. V. Chernomordik, J. D. Riley, M. Hassan, F. Amyot, B. Dasgeb, S. G. Demos, R. Pursley, R. F. Little, R. Yarchoan, Y. Tao, and A. H. Gandjbakhche, "Using noninvasive multispectral imaging to quantitatively assess tissue vasculature," *J. Biomed. Opt.* **12**, 051604 (2007).
14. N. Tsumura, H. Haneishi, and Y. Miyake, "Independent-component analysis of skin color image," *J. Opt. Soc. Am.* A **16**, 2169–2176 (1999).
15. J. O'Doherty, J. Henricson, C. Anderson, M. J. Leahy, G. E. Nilsson, and F. Sjöberg, "Sub-epidermal imaging using polarized light spectroscopy for assessment of skin microcirculation," *Skin Res. Technol* **13**, 472–484 (2007).
16. J. O'Doherty, P. McNamara, N. T. Clancy, J. G. Enfield, and M. J. Leahy, "Comparison of instruments for investigation of microcirculatory blood flow and red blood cell concentration," *J. Biomed. Opt.* **14**, 034025 (2009).

17. D. Nakao, N. Tsumura, and Y. Miyake, "Real-time multi-spectral image processing for mapping pigmentation in human skin," *IS&T/SID's 9th Color Imaging Conference, Color Science, Systems and Applications,* Scottsdale, AZ, pp. 80–84 (2001).

18. I. Nishidate, K. Sasaoka, T. Yuasa, K. Niizeki, T. Maeda, and Y. Aizu, "Visualizing of skin chromophore concentrations by use of RGB images," *Opt. Lett.* **33**, 2263–2265 (2008).

19. L.-H. Wang, S. L. Jacques, and L.-Q. Zheng, "MCML-Monte Carlo modeling of photon transport in multi-layered tissues," *Comput. Methods Programs Biomed.* **47**, 131–146 (1995).

20. S. L. Jacques, *Skin Optics*, see http://omlc.ogi.edu/news/jan98/skinoptics.html (1998).

21. S. L. Jacques, R. D. Glickman, and J. A. Schwartz, "Internal absorption coefficient and threshold for pulsed laser disruption of melanosomes isolated from retinal pigment epithelium," *Proc. SPIE* **2681**, 468–477 (1996).

22. S. A. Prahl, *Tabulated Molar Extinction Coefficient for Hemoglobin in Water*, see http://omlc.ogi.edu/spectra/hemoglobin/summary.html (1999).

23. S. L. Jacques, "Origins of tissue optical properties in the UVA, Visible, and NIR region," *OSA TOPS on Advances in Optical Imaging and Photon Migration*, R. R. Alfano and J. G. Fujimoto, Eds., Vol. **2**, pp. 364–369, Optical Society of America, Washington, DC (1996).

24. M. J. C. van Gemert, S. L. Jacques, H. J. C. M. Sterenborg, and W. M. Star, "Skin optics," *IEEE Trans. Biomed. Eng.* **36**, 1146–1154 (1989).

25. A. Knüttel and M. Boehlau-Godau, "Spatially confined and temporally resolved refractive index and scattering evaluation in human skin performed with optical coherence tomography," *J. Biomed. Opt.* **5**, 83–92 (2000).

26. P. D. Ninni, F. Martelli, and G. Zaccanti, "The use of India ink in tissue-simulating phantoms," *Opt. Express* **18**, 26854–26865 (2010).

27. D. Gniechwitz, N. Reichardt, J. Ralph, M. Blaut, H. Steinhart, and M. Bunzel, "Isolation and characterisation of a coffee melanoidin fraction," *J. Sci. Food. Agric.* **88**, 2153–2160 (2008).

28. H. Motai and S. Inoue, "Conversion of color components of melanoidin produced from the glycine-xylose system," *Agric. Bio. Chem.* **38**, 233–239 (1974).

29. A. Serban and A. Nissenbaum, "Light induced production of hydrogen from water by catalysis with ruthenium melanoidins," *Int. J. Hydrogen Energy* **25**, 733–737 (2000).

30. I. Nishidate, Y. Aizu, and H. Mishina, "Estimation of absorbing components in a local blood layer embedded in the turbid media on the basis of visible to near-infrared (VIS-NIR) reflectance spectra," *Opt. Rev.* **10**, 427–435 (2003).

31. I. Nishidate, T. Maeda, Y. Aizu, and K. Niizeki, "Visualizing depth and thickness of a local blood region in skin tissue using diffuse reflectance images," *J. Biomed. Opt.* **12**, 054006 (2007).

32. H. J. van Staveren, C. J. M. Moes, J. Marle, S. A. Prahl, and M. J. C. Gemert, "Light scattering in Intralipid-10% in the wavelength range of 400-1100 nm," *Appl. Opt.* **30**, 4507–4514 (1991).

33. Y. Higashi, S. Sasaki, K. Nakagawa, T. Ueda, A. Yoshimizu, S. Kurisu, H. Matsuura, G. Kajiyama, and T. Oshima, "A comparison of angiotensin-converting enzyme inhibitors, calcium antagonists, beta-blockers and diuretic agents on reactive hypermia in patients with essential hypertension: a multicenter study," *J. Am. Coll. Cardio* **35**, 284–291 (2002).

34. R. J. Cody, F. B. Müller, S. H. Kubo, H. Rutman, and D. Leonard, "Identification of the direct vasodilator effect of milrinone with an isolated limb preparation in patients with chronic congestive heart failure," *Circulation* **73**, 124–129 (1986).

35. D. E. Hokanson, D. S. Sumner, and D. E. Strandness, "An electrically calibrated plethysmograph for direct measurement of limb blood flow," *IEEE Trans. Biomed. Eng.* **22**, 25–29 (1975).

36. G. N. Stamatas, M. Southall, and N. Kollias, "*In vivo* monitoring of cutaneous edema using spectral imaging in the visible and near infrared," *J. Investigat. Dermatol.* **126**, 1753–1760 (2006).

37. G. N. Stamatas and N. Kollias, "*In vivo* documentation of cutaneous inflammation using spectral imaging," *J. Biomed. Opt.* **12**, 051603 (2007).

38. K. G. Brodovicz, K. McNaughton, N. Uemura, G. Meininger, C. J. Girman, and S. H. Yale, "Reliability and feasibility of methods to quantitatively assess peripheral edema," *Clin. Med. Res.* **7**, 21–31 (2009).